







Transverse Wave Induced Kelvin–Helmholtz Rolls in Spicules

P. Antolin¹ , D. Schmit^{2,3}, T. M. D. Pereira^{4,5} , B. De Pontieu^{2,4,5} , and I. De Moortel¹ 

¹ School of Mathematics and Statistics, University of St. Andrews, St. Andrews, Fife KY16 9SS, UK; patrick.antolin@st-andrews.ac.uk

² Lockheed Martin Solar and Astrophysics Laboratory, B/252, 3251 Hanover Street, Palo Alto, CA 94304, USA

³ Now at: Catholic University, Department of Physics, 620 Michigan Avenue, N.E., Washington, DC 20064, USA

⁴ Roseland Centre for Solar Physics, University of Oslo, P.O. Box 1029 Blindern, N-0315 Oslo, Norway

⁵ Institute of Theoretical Astrophysics, University of Oslo, P.O. Box 1029 Blindern, N-0315 Oslo, Norway

Received 2017 June 22; revised 2018 February 12; accepted 2018 February 26; published 2018 March 23

Abstract

In addition to their jet-like dynamic behavior, spicules usually exhibit strong transverse speeds, multi-stranded structure, and heating from chromospheric to transition region temperatures. In this work we first analyze *Hinode* and *IRIS* observations of spicules and find different behaviors in terms of their Doppler velocity evolution and collective motion of their sub-structure. Some have a Doppler shift sign change that is rather fixed along the spicule axis, and lack coherence in the oscillatory motion of strand-like structure, matching rotation models, or long-wavelength torsional Alfvén waves. Others exhibit a Doppler shift sign change at maximum displacement and coherent motion of their strands, suggesting a collective magnetohydrodynamic (MHD) wave. By comparing with an idealized 3D MHD simulation combined with radiative transfer modeling, we analyze the role of transverse MHD waves and associated instabilities in spicule-like features. We find that transverse wave induced Kelvin–Helmholtz (TWIKH) rolls lead to coherence of strand-like structure in imaging and spectral maps, as seen in some observations. The rapid transverse dynamics and the density and temperature gradients at the spicule boundary lead to ring-shaped Mg II k and Ca II H source functions in the transverse cross-section, potentially allowing *IRIS* to capture the Kelvin–Helmholtz instability dynamics. Twists and currents propagate along the spicule at Alfvénic speeds, and the temperature variations within TWIKH rolls, produce the sudden appearance/disappearance of strands seen in Doppler velocity and in Ca II H intensity. However, only a mild intensity increase in higher-temperature lines is obtained, suggesting there is an additional heating mechanism at work in spicules.

Key words: instabilities – magnetohydrodynamics (MHD) – Sun: activity – Sun: chromosphere – Sun: corona – Sun: oscillations

Supporting material: animations

1. Introduction

Spicules are chromospheric jets protruding into the corona, ubiquitously found on the Sun. Properties such as dynamics, morphology, and heating suggest that these jets may play a substantial role as energy conduits to the corona (De Pontieu et al. 2011).

Two types of spicules have been proposed (De Pontieu et al. 2007a), both of which exhibit strong transverse (combining swaying and torsional) motions (Pereira et al. 2012, 2016; Sekse et al. 2013; De Pontieu et al. 2014a). Type I spicules typically show full parabolic paths in chromospheric lines, with velocities on the order of 15–40 km s^{−1} and lifetimes of about 3–10 minutes (Pereira et al. 2012). Type II spicules differ from their type I counterparts in terms of the faster observed longitudinal speeds (30–100 km s^{−1}), their rapid disappearance in the Ca II H passband but increase in visibility in higher-temperature emission lines (De Pontieu et al. 2009; Pereira et al. 2014; Rouppe van der Voort et al. 2015), and their multi-stranded structure (Suematsu et al. 2008a; Skogsrud et al. 2014).

In high-resolution tunable Fabry–Pérot instruments such as SST/CRISP, rapid disappearance of the entire structure for type II spicules in high blueshift and redshift positions is observed, suggesting very high, even non-physical, propagation speeds (Kuridze et al. 2015; Pereira et al. 2016; Shetye et al. 2016). This fact has led to consideration of different interpretations for spicule formation, such as the combination of different lines of sight (LOSs) and the expected curved shape of chromospheric current sheets within flux tubes (Judge et al. 2012). This sudden

appearance and disappearance in narrow passbands at high blueshifts and redshifts, observed throughout the solar disk and off-limb, cannot be explained by a simple geometric expansion of the loop combined with very fast longitudinal speeds (Sekse et al. 2013; Pereira et al. 2016). The observed transverse swaying and torsional component in spicules (of the order of 25–30 km s^{−1}) was proposed as an explanation for this effect (De Pontieu et al. 2012), a motion that could be caused by a mix of torsional Alfvén and kink-mode waves. This sudden appearance and disappearance in narrow passbands produces contiguous strand-like structure of spicules in Doppler maps, with opposite velocities along their entire lengths, and with a high-frequency oscillatory change in the Doppler signal. The torsional Alfvén wave interpretation for this effect was recently supported by Srivastava et al. (2017). The latter work lacks, however, any forward modeling, and a clear link between the numerical modeling cannot be established with the observations.

While general consensus exists for the generation mechanism of type I spicules being longitudinal slow modes steepening into shocks (De Pontieu et al. 2005), there is no work that fully reproduces type II spicules. The 3D magnetohydrodynamic (MHD) models of Martínez-Sykora et al. (2013) and Iijima & Yokoyama (2017), encompassing both the sub-photospheric region and corona, manage to generate spicules with significant transverse displacements (and rotational components) from reconnection at photospheric heights combined with a slingshot effect by the Lorentz force. However, little strand-like structure in intensity and Doppler

is obtained, and the characteristic disappearance in the Ca II H band is not achieved. On the other hand, the recent model of Martinez-Sykora et al. (2017) shows that ambipolar diffusion may be the key to the generation of type II spicules. The addition of this mechanism increases the magnitude of the Lorentz force and the ensuing slingshot effect, thereby nonlinearly generating a strong enough slow-mode shock that pushes the mass upward (the spicule). Accompanying strong currents and thermal fronts are produced from the Alfvénic perturbations, which lead to heating to the transition region and coronal temperatures (and disappearance of Ca II H emission) during the lifetime of the spicule (De Pontieu et al. 2017a), and to fast apparent propagation (De Pontieu et al. 2017b), potentially explaining the observed fast plane-of-the-sky velocities in transition region lines (Tian et al. 2014; Narang et al. 2016). However, the model is limited to 2.5D MHD with low spatial resolution. Hence, the dynamic instabilities and turbulence associated with transverse MHD waves and resonant absorption, which are expected to play a role in the spicule morphology and thermodynamic evolution, are not captured. It is therefore unclear how much of the observed type II spicule characteristics can be reproduced with this model, particularly concerning the observed variability in the Doppler signal.

Transverse MHD waves are observed in the solar atmosphere (De Pontieu et al. 2007b; Tomczyk et al. 2007; Arregui et al. 2012; De Moortel & Nakariakov 2012) and constitute one of the prime coronal heating candidates, thanks to their ability to carry large amounts of energy into the corona (see, e.g., the review by Arregui 2015). Many of these energy estimates (and therefore much of the heating candidate status) are actually based on observations of these waves in the chromosphere, and particularly along spicules (De Pontieu et al. 2007b; He et al. 2009; Jess et al. 2012; Pereira et al. 2012, 2016; Kuridze et al. 2016), where large amplitudes of tens of km s^{-1} are usually observed. Such transverse, wave-like motions of spicules constitute a key observed property of these phenomena.

Transverse MHD waves can easily trigger the Kelvin–Helmholtz instability (KHI; Terradas et al. 2008; Antolin et al. 2014; Magyar & Van Doorselaere 2016), with vortices excited mostly in the transverse plane to the loop axis. These 3D vortices are known as transverse wave induced K–H (TWIKH) rolls, and generate a turbulent-like regime in which energy can be dissipated through viscosity and resistivity (Magyar & Van Doorselaere 2016; Howson et al. 2017b). Recently, a new turbulent regime from unidirectional Alfvénic waves has been discovered, which relaxes the condition of having counter-propagating waves for the onset of turbulence (Magyar et al. 2017). Although the KHI is produced preferentially in the absence of an inhomogeneous boundary due to the short spatial scales of the shear (Terradas et al. 2008), the presence of an inhomogeneous layer can maintain the KHI for longer times. Indeed, the resonant absorption mechanism associated with transverse MHD waves continuous to act until the global kink mode is fully damped (Goossens et al. 2002). A continuous driving of these waves, as investigated by Karamelas et al. (2017), is observed to completely deform the original flux tubes and leads to heating preferentially by Ohmic dissipation toward the footpoints. The high longitudinal speeds observed in type II spicules also suggest that the KHI wave vectors have an important

longitudinal component (Ajabshirizadeh et al. 2015; Zaqrashvili et al. 2015; Zhelyazkov et al. 2015), leading to helical TWIKH rolls that could be responsible for observed vortex-like structure (Kuridze et al. 2016).

In this work we analyze and compare spicules observed with *Hinode* (Kosugi et al. 2007) and the *Interface Region Imaging Spectrograph* (*IRIS*; De Pontieu et al. 2014b) with a high-resolution 3D MHD model of a spicule-like feature subject to transverse MHD waves. Our aim is not to model the generation of a spicule, but to study the effect that these waves may have on the spicule during its lifetime, and identify which observational characteristics can be attributed to their presence. Such kink waves may be produced by the spicule driver (He et al. 2009; Jess et al. 2012), as in the recently proposed model driven by ambipolar diffusion of Martinez-Sykora et al. (2017) which, however, does not include the high-resolution modeling, wave mode coupling, and the associated dynamic instabilities we consider here.

2. Observations

2.1. *IRIS* and *Hinode* Coordinated Observations

IRIS and *Hinode* co-observed at the north limb between 2014 April 29 01:00 UT and 02:00 UT (IHOP 249). The *IRIS* observing program ran between 2014 April 28 22:39 UT and April 29 02:58 UT, with the *IRIS* slit centered at helioprojective coordinates $(-4, 959)$. *IRIS* was rolled 90° so that the slit was parallel to the limb and with the middle of the slit $7''$ off the limb. The *IRIS* slit-jaw imager (SJI) and spectrograph (SG, in sit-and-stare mode) observed with cadences 19 s (SJI) and 9.5 s (SG) with an exposure of 8 s (and 1.5 s readout time). The observing program included the SJI 1400 and 2796 channels, which provide passband filtered images centered on the emission lines of Si IV at 1402.77 \AA and Mg II k at 2796.35 \AA , respectively. The SJI instrument observed with a field-of-view (FOV) of $120'' \times 120''$ and $0.''166 \text{ pix}^{-1}$ platescale. The *IRIS* slit was $0.''33$ wide. For analysis, we used level 2 data (De Pontieu et al. 2014b) and corrected for thermal variations of the pointing by co-aligning each image using a cross-correlation maximization routine. We found that the *IRIS* data drifts by $3''$ over the 60 minutes of observations overlapping with the *Hinode* Solar Optical Telescope (SOT) observing period. The *IRIS* spectrograph had 25 mÅ platescale and 53 mÅ resolution in the NUV. The spectral profiles of the spicules at the slit height exhibited few reversals on average and were fitted as Gaussians using a least-squares minimization algorithm. Profile fits with a high χ^2 were discarded.

SOT (Suematsu et al. 2008b; Tsuneta et al. 2008) observed between 2014 April 29 01:00 UT and 02:00 UT with a cadence of 4.8 s (1.8 s exposure). SOT observed a $56'' \times 56''$ FOV with $0.''11 \text{ pix}^{-1}$ platescale. The entire SOT FOV is included in the *IRIS* FOV. The SOT data set was processed using the FG_PREP Solarsoft routine, which flat fields and dark subtracts the data. Over the 60 minutes of observations, our data set drifted approximately $6''$ southwest, which we corrected using a linear offset function.

Three parameters (rotation angle, x -center, and y -center) were varied to arrive at alignment parameters which matched both the x - y images (the Mg II k at 2796.35 \AA and Ca II H at 3969.59 \AA lines are formed in similar regions of the atmosphere) and time–distance plots using visual inspection. Because of the drift in each data series and our parameterized correction,

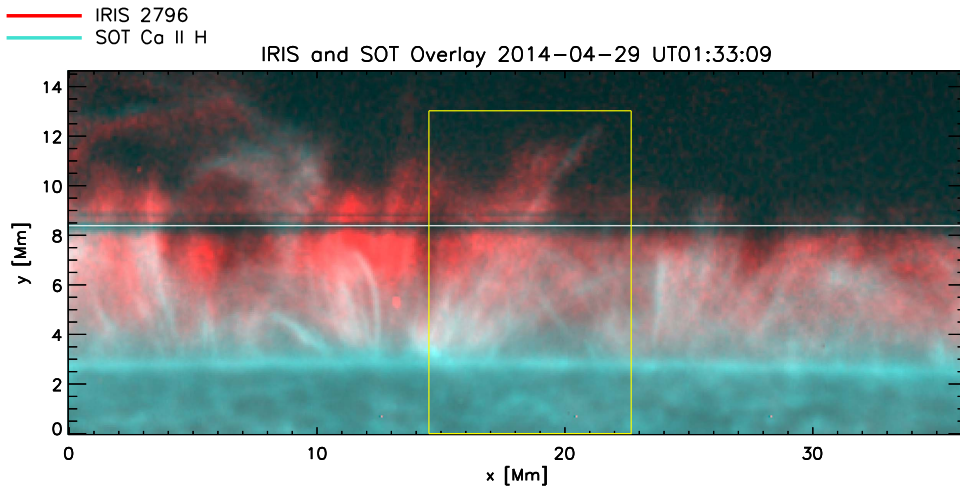


Figure 1. *Hinode* and *IRIS* observations of spicules. Composite image of *IRIS* SJI 2796 (red) and SOT Ca II H line (turquoise). The FOV corresponding to Figure 2 is marked by the yellow square. The *IRIS* slit location is marked by the horizontal white line. In the animated movie corresponding to this figure the FOVs of the cases shown in Figure 3 also appear in a yellow square at the time of occurrence.

(An animation of this figure is available.)

we estimated the co-alignment of the *IRIS* and SOT data sets to be accurate to $0''.5$.

2.2. Spectral Analysis of Spicules

In Figure 1 most of the overlapping FOV between *IRIS* and *Hinode*/SOT is shown, in which the *IRIS* slit sits on top of spicules. The yellow square in the figure corresponds to the FOV shown in Figure 2. What appears to be a collection of spicules (see the arrows in Figure 2) at high resolution with SOT in Ca II H emanates from a bright region on the disk, extending for about 12 Mm with an upward instantaneous speed of 25 km s^{-1} . Although some sub-structure is also seen with SJI 2796, the collection of strands is mostly seen as a single monolithic structure in that passband. Some sub-structure is seen in SJI 1400, but the monolithic structure is less clear. As the structure extends upwards along an inclined trajectory, the inner strands are also seen to oscillate in the transverse direction. This sideways motion appears coherent for the set of strands (or spicules) over a transverse length of about 3 Mm, and also along their length, suggesting either a collective standing wave (no upward propagating wavefront is observed) or a long-wavelength propagating wave. The oscillation is clearly seen for about one period $\approx 250 \pm 20 \text{ s}$. During the second half of the oscillation period the collective set of strands brightens simultaneously at all wavelengths. The strand at the right boundary of this group is the brightest and marks the right boundary of the monolithic structure seen in Mg II (and in Si IV, but less clearly). After this single-period motion the whole group fades out in the Ca II H passband, but remains visible in Mg II (and barely in Si IV), a change in visibility that is typical of type II spicules (Skogsrud et al. 2015). Later on, the spicule group decreases in intensity at all wavelengths and the downward parabolic trajectory is barely visible. Other spicules with different inclination also come into the same LOS, making the follow-up dynamic motion difficult to track.

Coinciding with the time of both (right- and left-most) maximum transverse displacements, the Doppler shifts change sign with average values between -10 and 10 km s^{-1} (and maxima around 15 km s^{-1}). Although the group of strands

appears coherent, the Doppler shift transition (sign change) is ragged, being at slightly different times across the width of the group. The line width across the group shows an enhanced value of $\approx 12 \text{ km s}^{-1}$, about $3\text{--}5 \text{ km s}^{-1}$ above the background. Within the group, the bright right-most strand stands out, with enhanced values up to 19 km s^{-1} .

In Figures 3 and 4 we show four other spicule cases. Case 2 in Figure 3 shows a similar case as in Figure 2, in which, however, an outward propagating transverse displacement is observed (time–distance cuts at different heights show propagating wavefronts, not shown here). The intensity and spectral features appear very similar, albeit shorter lived.

As for case 1, case 3 in Figure 3 and cases 4 and 5 in Figure 4 exhibit strand-like structure and rapid disappearance in Ca II H, together with persistent, monolithic structure in 2796 and 1400 (with some signatures of strand-like structure). However, the collective motion of the strands is mostly seen out-of-phase and exhibits similar patterns as those reported by Okamoto et al. (2016) for rotation in a prominence. In particular, the Doppler velocity transitions are oriented roughly along the spicule axis, with one side of the strand group having a distinct blue- or redshifted velocity, opposite to the other side.

These five events illustrate the complexity of multi-wavelength spectroscopic observations of spicules. To make sense of these observations, and particularly the observed difference in the Doppler shifts, it is important to first have a top-level view of what kind of patterns to expect in the data, based on the usual agents that are commonly invoked to explain the observed wave-like dynamics, such as transverse MHD waves, torsional Alfvén waves, and rotation. We will then first use simple models of these likely scenarios before performing numerical simulations.

2.3. A Gedanken Model of Spicule Oscillations

In Figure 5 we schematically show the time–distance diagrams of what would be expected from commonly considered scenarios for explaining the observed cases 1–5, particularly concerning the distinct Doppler velocities. We consider two kink wave models (the “classic” kink mode and TWIKH rolls model, corresponding respectively to models

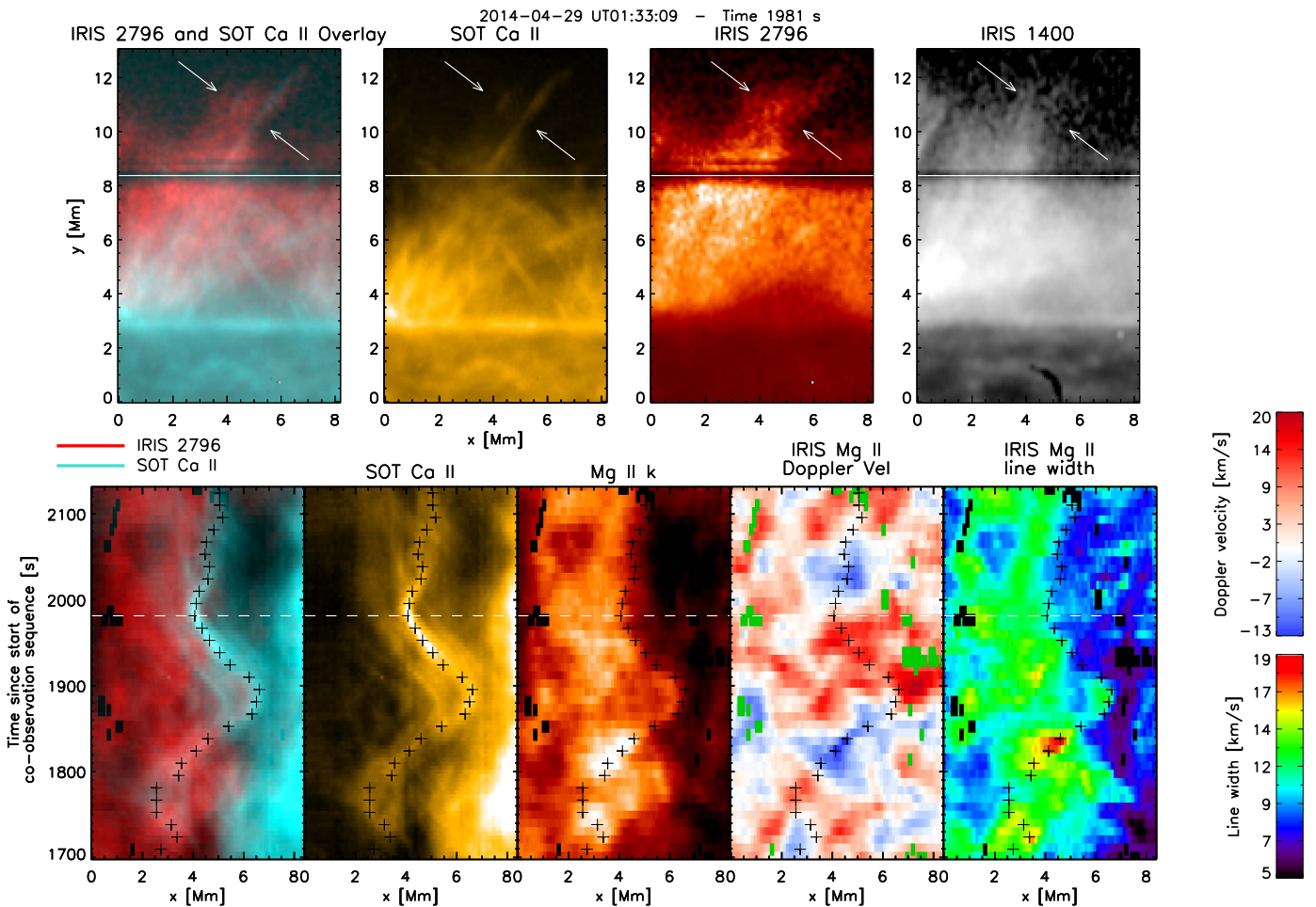


Figure 2. *Hinode* and *IRIS* observations of spicules. Top panels: from left to right, composite image of *IRIS* SJI 2796 (red) and SOT Ca II H line (turquoise), the corresponding SOT image in the Ca II H line (yellow), the SJI 2796 image (red), and the SJI 1400 image (gray). In these images a spicule group is observed (marked with arrows). Bottom panels: from left to right, time–distance diagrams at the *IRIS* slit location (horizontal white line on top panels) for the composite intensities of *IRIS* SJI 2796 (red) and SOT Ca II H line (turquoise), the SOT Ca II H line intensity (yellow), the SJI 2796 intensity (red), the Doppler velocity, and line width in Mg II k. For the SOT intensity diagram we have summed over several cuts perpendicular to the oscillating structure, along 2 Mm length from the location of the *IRIS* slit crossing and above. The black crosses denote locations of maximum Ca II intensity within the spicule group. Green/black pixels in the Doppler/line width maps denote regions too dim to retrieve a quality fit. See also the accompanying animation for this figure.

(An animation of this figure is available.)

with and without associated dynamic instabilities and resonant absorption), a torsional Alfvén wave model, a rotation model, and combinations of each of these models with a kink, assuming that the amplitudes of the torsional and rotational motions dominate.

Although it is unclear at this point what the strand-like structure would correspond to in these models, the Doppler shifts show a distinct behavior. The models involving rotation have a Doppler shift transition that is roughly fixed in space, leading to an asymmetry of blueshift and redshift from left to right of the spicule, potentially matching cases 3, 4, and 5 (cases 3 and 4 seem to combine as well an additional transverse component, such as that produced by a coupling of rotation with a kink mode). This behavior could also correspond to a propagating long-wavelength torsional Alfvén wave (assuming we see only half a period or less). The observed Doppler shift transition of cases 1 and 2 is only obtained in the kink mode and partly the torsional Alfvén mode. However, for the latter we should observe a periodic asymmetry for half or part of the flux tube, which is not observed. The kink mode, being a collective mode, is particularly well suited for explaining the

collective motion of the strand-like structure. On the other hand, to explain the strong collective transverse motion by a torsional Alfvén mode, the strands would need to be on a shell of constant Alfvén speed within the flux tube, and the wavelength would need to be much longer than the spicule length. This configuration could be expected to lead to small Doppler shifts due to the sum over the many expected shells with different Alfvén speeds within a flux tube (phase mixing, particularly in conditions not far from optically thin), combined with an increase of line width toward the edges, which is not observed. However, in the case of a spectral line having a source function peaking in a shell in the boundary (ring-shaped when taking a cross-section of the loop) a collective strand motion with high Doppler shifts may be possible. Indeed, such a source function would act as a preferential visual filter for the torsional Alfvén waves within the shell delimited by the source function. As we will see from our model, such source functions are possible, and only a 3D MHD simulation of the torsional Alfvén wave mechanism, combined with forward modeling, would allow us to properly assess this possibility.

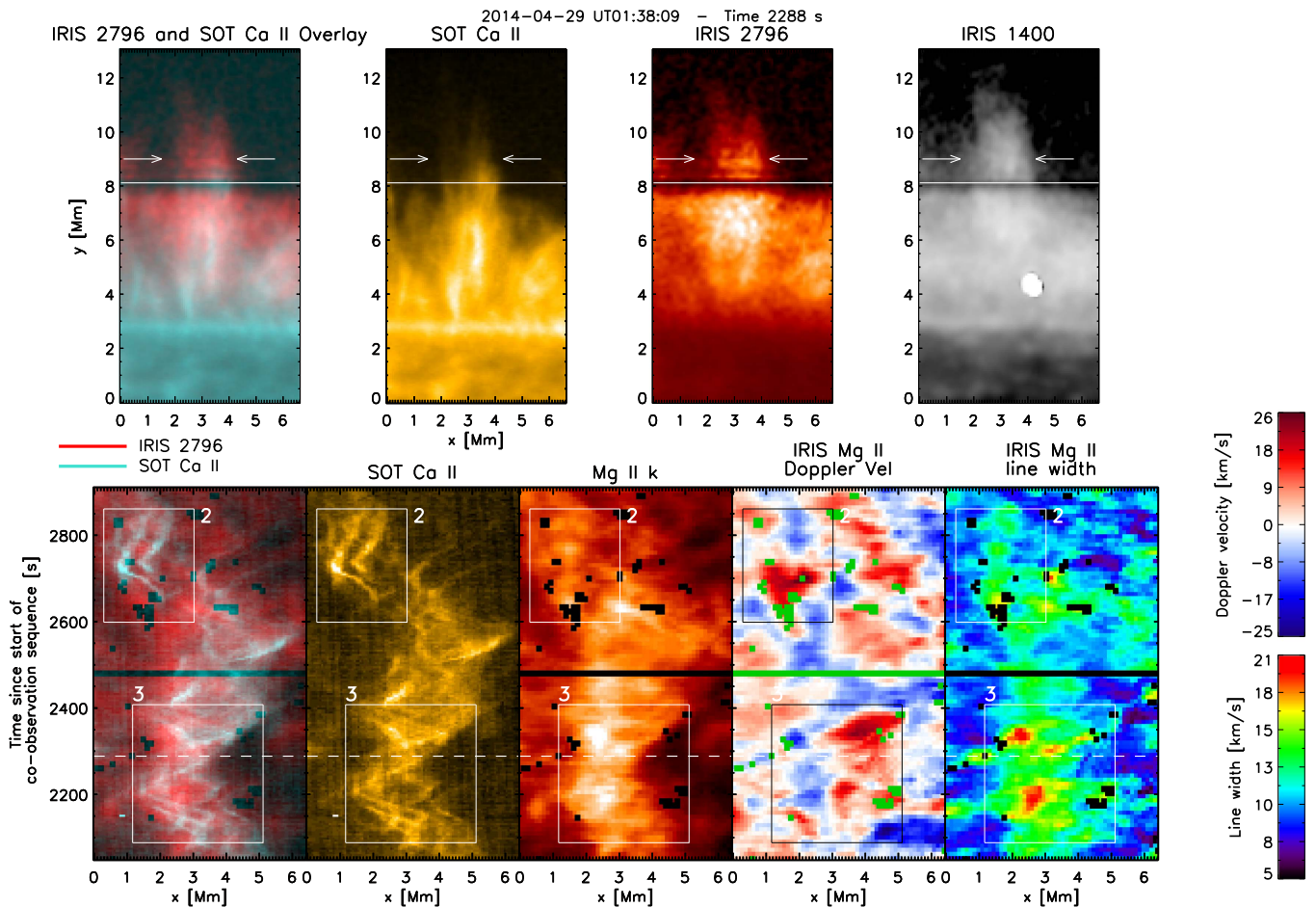


Figure 3. *Hinode* and *IRIS* observations of spicules. Similarly to Figure 2 (case 1), we show here two other cases of spicule groups: one subject to a propagating kink wave (case 2), and another subject to a rotation or a torsional Alfvén wave (case 3). See also the accompanying animation for this figure.

(An animation of this figure is available.)

In this paper we concentrate on the effect of the kink wave. We will focus particularly on case 1 and check with a 3D MHD simulation, as the simple cartoon suggests, that a flux tube oscillating with a transverse MHD wave can explain the observed Doppler shifts, as well as the other spectral characteristics.

3. Numerical Modeling

As mentioned in the introduction, transverse, wave-like motions are a key property of spicules that cannot be explained by a combination of geometry and their longitudinal up/down motions alone. For the sake of simplicity we assume that we can isolate the transverse motion from the longitudinal motion in order to study the effect that transverse MHD waves have on the observable properties of spicules. In this work we therefore do not focus on the generation mechanism of spicules but assume that we have initially a static spicule at the footpoint of a loop.

3.1. Numerical Model

As shown in Figure 6 we model what can be considered a typical spicule (Tsiropoula et al. 2012) with a dense and cold core with $n_i = 50 n_e$ and $T_i = \frac{1}{100} T_e$, where n and T denote the total number density and temperature, and i, e denote the internal and external values, respectively. We take initially

$T_i = 10^4$ K, $n_i = 6 \times 10^{10} \text{ cm}^{-3}$, values commonly found in spicules. The density is given by $\rho = \mu m_p n$, where μ is the mean molecular weight and m_p the proton mass. To keep pressure balance throughout the atmosphere, the magnetic field varies slightly from $B_i = 14.5$ G to $B_e = 14.43$ G, and the plasma β is 0.02 everywhere. The boundary layer connecting the internal and external values follows the equation:

$$\rho(x, y) = \rho_e + (\rho_i - \rho_e)\zeta(x, y), \quad (1)$$

where

$$\zeta(x, y) = \frac{1}{2} \left(1 - \tanh \left(b \left(r(x, y) - \frac{1}{2} \right) \right) \right). \quad (2)$$

The coordinates x and y are in the plane perpendicular to the loop axis, and z is along the axis. The $r(x, y) = \sqrt{x^2 + y^2}/w$ term denotes the normalized distance from the loop center and $w = 1$ Mm denotes the loop width. We therefore assume that our spicule and loop have a circular cross-section with an inhomogeneous boundary layer. We set $b = 16$, leading to a boundary layer width of ≈ 200 km. The loop has length $L = 100$ Mm.

The upper boundary of the spicule is a transition region to the corona. The internal and external temperatures change

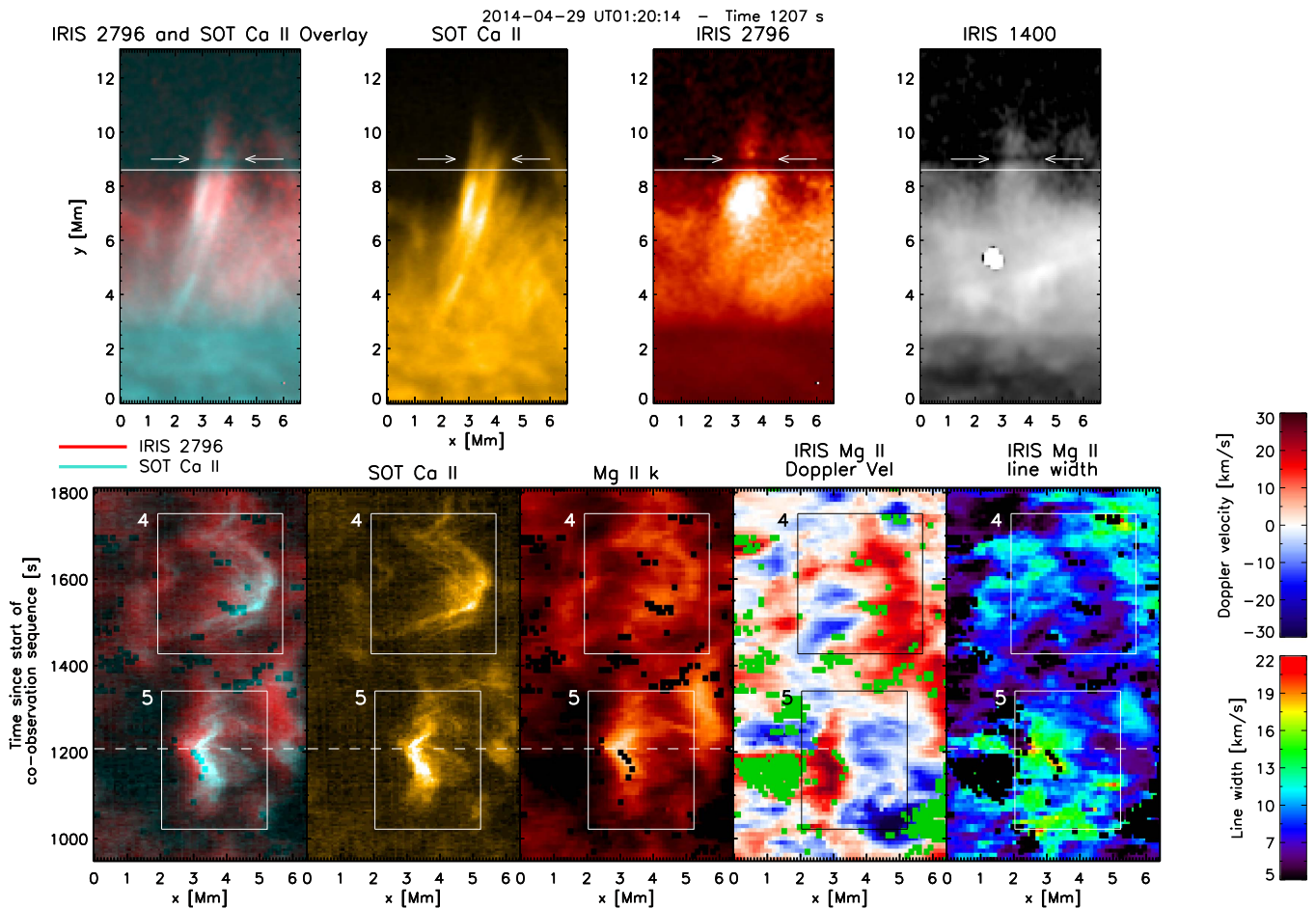


Figure 4. *Hinode* and *IRIS* observations of spicules. Similarly to Figure 2 (case 1), we show here two other cases of spicule groups, subject to a rotation or a torsional Alfvén wave (cases 4 and 5). See also the accompanying animation for this figure.

(An animation of this figure is available.)

everywhere with height according to:

$$T_{i,e}(z) = T_{i,e}(0) + T_{tr} \left(1 - \tanh \left(\frac{z - z_{tr}}{w_{tr}} \right) \right), \quad (3)$$

where $T_{i,e}(0)$ are the internal, external temperatures at height $z = 0$, $T_{tr} = 4.5 \times 10^5$ K, and $z_{tr} = 15$ Mm and $w_{tr} = 2$ Mm are the midpoint and extent of the transition region. The internal and external coronal temperatures are 0.91×10^6 K and 1.9×10^6 K. The loop has only an extremely mild density enhancement of 1.044 in the corona, leading to a value of $n_i = 6.3 \times 10^8 \text{ cm}^{-3}$, and would thus be indistinguishable from the surrounding (diffuse) corona. The initial cross-section and longitudinal variation along the x - z plane can be seen in the animation corresponding to Figure 6.

Following case 1, the flux tube is driven with a fundamental kink mode by imposing a transverse perturbation along the loop according to $v_x(x, y, z) = v_0 \cos(\pi z/L) \zeta(x, y)$, where $v_0 = 33 \text{ km s}^{-1}$ is the initial amplitude (at the loop apex), corresponding to 12 km s^{-1} in the top part of the spicule. We have chosen the same (x, y) dependence as that of the density in order to maximize the amount of energy given to the fundamental mode, and minimize the generation of other longitudinal modes. The chosen amplitude values are usually found in spicules, and are much lower than the observed

maximum speeds (on the order of 60 km s^{-1} ; Pereira et al. 2012). The kink phase speeds at spicular level and corona are 256 km s^{-1} and 1756 km s^{-1} , respectively.

A parameter space investigation was performed for our model, by changing the density (and temperature) contrast, the magnetic field strength, the initial velocity perturbation (amplitude and localization of the perturbation), and also the shape of our flux tube (multi-stranded structure instead of monolithic). Although various differences are seen (mainly concerning the amplitude of the driver), the physical mechanisms described here remain largely the same.

3.2. Numerical Setup

The 3D MHD simulation is performed with the CIP-MOCCT scheme (Kudoh et al. 1999). The MHD equations exclude gravity, loop expansion, and curvature since we focus on the transverse dynamics observed in spicules, for which we assume they are second-order factors. Furthermore, the effects of radiative cooling and thermal conduction are not included. The numerical grid contains $512 \times 256 \times 100$ points in the x , y , and z directions respectively. Thanks to the symmetric properties of the kink mode only half the plane in y and half the loop are modeled (from $z = 0$ to $z = 50$ Mm), and we set symmetric boundary conditions in all boundary planes except for x , where periodic boundary conditions are imposed. To minimize the influence from lateral boundary conditions, the

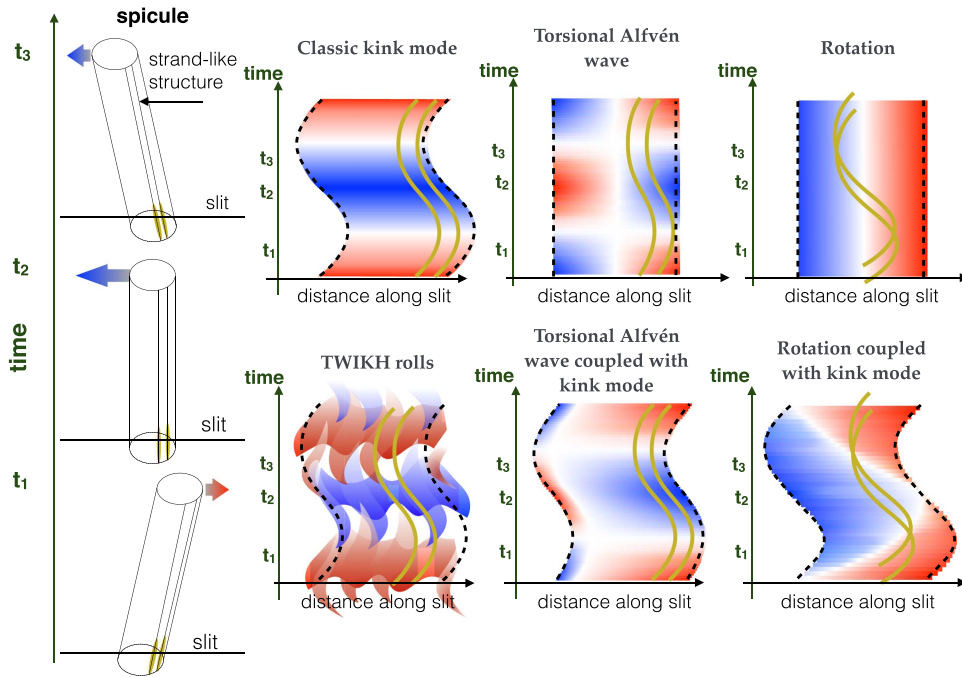


Figure 5. Sketch of time–distance diagrams of Doppler velocities for various considered models. The spicule is viewed from the side, as in Figure 7. The strand-like structure within the spicule (in yellow) has Doppler signatures (yellow paths) in the time–distance diagrams. In the torsional Alfvén wave case we only show a “shell” where the Alfvén speed is constant.

spatial grids in x and y are uniform with a resolution of 7.8 km where the loop dynamics are produced, and increase further away leading to a maximum distance of ≈ 8 Mm from the loop center. The simulation is close to ideal with no explicit resistivity or viscosity. From a parameter study, we estimate that the effective Reynolds and Lundquist numbers in the code are of the order of 10^4 – 10^5 (Antolin et al. 2015, 2017). The temporal variation in temperature in our model is therefore mostly due to adiabatic effects.

3.3. Spectral Synthesis

We synthesized spectra from the model to compare with observations. Calculations were carried out in two regimes: using the optically thin approximation with the FoMo code (Van Doorselaere et al. 2016) for the Si IV, Mg II k, and Ca II H lines, and by solving the full non-local thermal equilibrium (non-LTE) radiative transfer problem with partial frequency redistribution on a column-by-column basis with the RH 1.5D code (Uitenbroek 2001; Pereira & Uitenbroek 2015) for the Ca II and Mg II lines. Both approaches were done for comparison and for facilitating the calculations (optically thin over radiative transfer) when appropriate.

The MHD simulation does not explicitly calculate the electron density n_e , and to obtain self-consistent values of n_e for the non-LTE radiative transfer calculations we employ a two-step process. First, we solve the non-LTE problem for a five-level plus continuum hydrogen atom, using the Saha–Boltzmann equation to calculate n_e . This gives us the non-LTE hydrogen populations and ionization fraction, which are then used to calculate a consistent n_e in a second run where we solve the non-LTE problem simultaneously for a Mg II and a Ca II atom. We use the five-level plus continuum model Mg II atom of Leenaarts et al. (2013a), and a similar five-level plus continuum Ca II atom. In both cases we allow for partial redistribution (PRD) in the lines of interest (Mg II h and k,

Ca II H), and use the fast angle-dependent PRD approximation of Leenaarts et al. (2012).

The 1.5D approach was used to avoid the large computational burden of full 3D calculations. This approximation breaks down near the line cores (Leenaarts et al. 2013b), but because we work with line-integrated quantities or whole line fits, the approximation is likely reasonable. With relatively low column masses in the model, the photon mean free path can be large compared with the cell size. Sharp temperature or density variations can induce large spatial variations in spectra from 1.5D calculations, when compared with 3D results that include diffusion from inclined rays. To mitigate for this effect, we spatially convolved the spectra from RH 1.5D with a Gaussian, and chose a conservative FWHM of 50 km to mimic the typical diffusion in integrated line intensities. This value is based on estimates of the photon mean free path for the Mg II h and k lines in the chromosphere (Leenaarts et al. 2013a). For calculating the source function of the Mg II k line we mimic the *IRIS* filter transmission function by using a Gaussian with 4 Å FWHM and centered at 2796.3 Å. For Ca II H we use the BFI filter transmission function given by *Solar SoftWare*.

4. Results

4.1. Development of the Numerical Experiment

The loop oscillates with a period of ≈ 255 s (see Figure 6), in agreement with the expected fundamental period (considering the different travel times along the loop) of $2(L_c/c_{k,c} + 2L_{ch}/c_{k,ch} + 2L_{tr}/c_{k,tr}) \approx 255$ s, where L_c , L_{ch} , and L_{tr} denote the lengths of the corona, spicule and transition region, respectively (and $c_{k,tr}$ is an average between the coronal and chromospheric kink speeds). Besides the fundamental mode, higher harmonics and slow and fast propagating modes are produced along the loop. This is particularly evident along the spicule, which sustains its own trapped modes at high

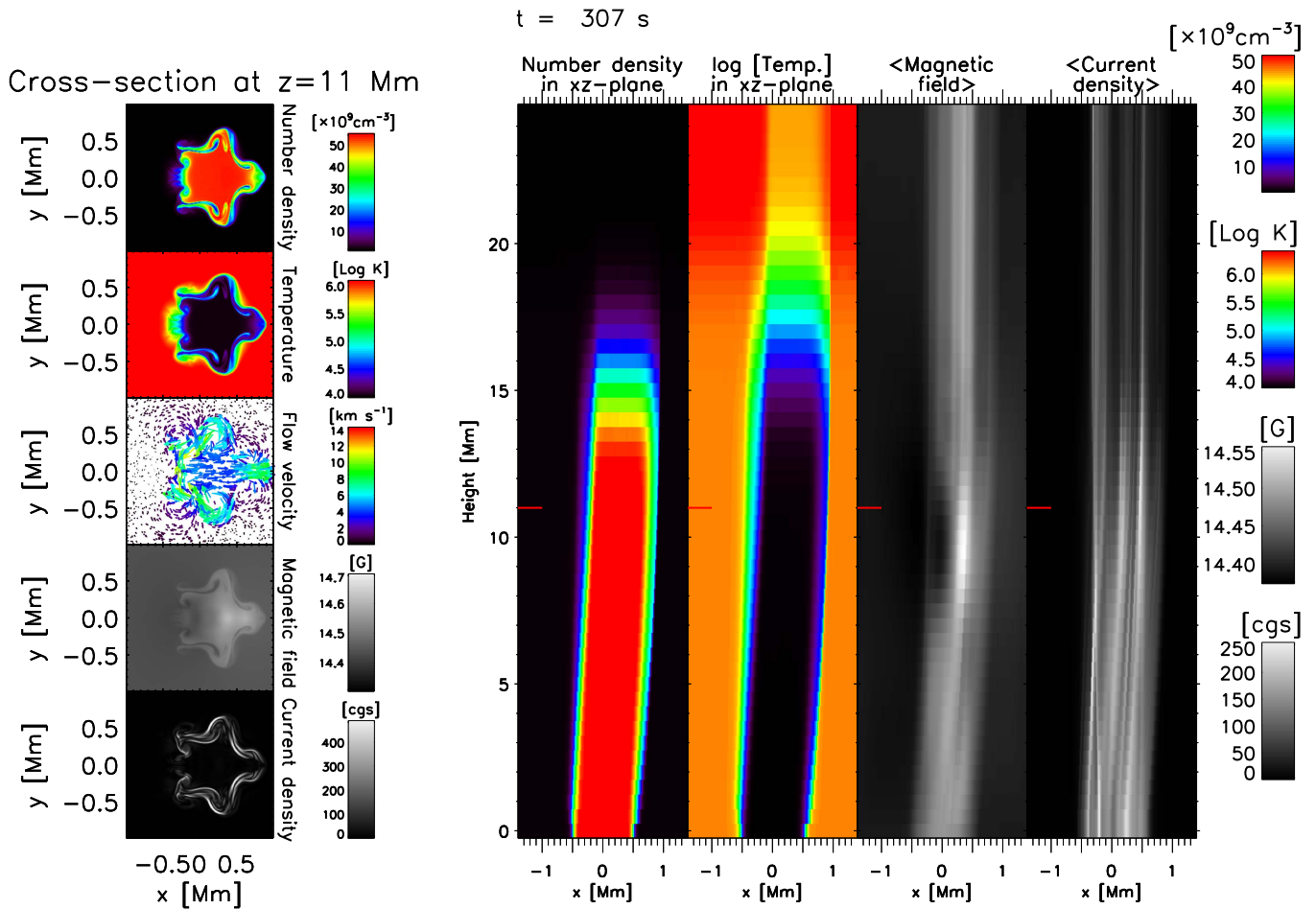


Figure 6. Spicule model. Four-set on right: side view of the simulated spicule along the (x, z) plane (plane of oscillation at $y = 0$) for the number density and temperature (in log values), and the average along the y axis for each (x, z) coordinate for the magnetic field strength and current density. Five-set on left: perpendicular cross-section of the spicule at a height of $z = 11 \text{ Mm}$ for the same quantities, including the flow velocity. See also the accompanying animation for this figure.

(An animation of this figure is available.)

frequencies due to the rapidly changing density at the transition region (see the magnetic field panel in Figure 6).

After half a period we notice the formation of TWIKH rolls all along the loop. The vortices fully develop first in the corona, and about 10–20 s later at chromospheric level. The vortices occur not only at the sides (facing the y direction), but also in the wake of the loop, due to the large velocity amplitude. The vortices at the wake result from the convergence of the azimuthal flow at the wake (see the density and vorticity panels in Figure 9), where it becomes unstable. The oppositely directed azimuthal flow is mainly driven by azimuthal Alfvén waves from resonant absorption and from the inertia of the flux tube, which compresses the front and adds momentum to the flow. Finger-like structures are generated at the wake, which end up curling before moving in the opposite direction. These vortices seem to combine a Rayleigh–Taylor nature and Alfvénic vortex shedding (Gruszecki et al. 2010).

TWIKH rolls twist the magnetic field. Because of the variation of the amplitude of the vortices with height (increasing on average) the twist also varies with height. This differential twist in the longitudinal direction propagates as azimuthal Alfvén waves along the loop, nonlinearly generating longitudinal ponderomotive forces that drive downward and upward flows. This is shown in Figure 7, where an upward

propagating twist that has previously reflected at the lower boundary can be seen in the spicule. Although a full representation of this twist would require a follow-up of the 3D geometry of the magnetic field, here we show only a planar cut through the twist in the y – z plane. The x – y cross-section of this twist can be further inspected in Figures 6 and 9 and the accompanying animations. This twist, which constitutes a variation of the magnetic field strength of about 0.2 G (with maxima up to 0.7 G), generates an upward force leading to flows of 5 – 10 km s^{-1} . This can also be understood by order of magnitude estimates, since $v_s/v_A \approx B_\phi/B \approx 0.01$ – 0.05 , where v_s is the longitudinal flow generated by the transverse perturbation B_ϕ from the twist on the field B , and the Alfvén speed v_A is on the order of 200 – 300 km s^{-1} at the location of Mg II formation (within the boundary of the flux tube). The twist is accompanied by currents that will be associated with heating in a non-adiabatic model taking into account resistive and viscous dissipation. While the exact amount of heating would depend on local parameters such as density, the magnetic field strength and resistivity, assuming full dissipation of the Alfvénic wave associated with a twist of 0.7 G would lead to an increase of 0.1–1 MK for a plasma density at the spicule boundary or in the corona of 10^9 – 10^8 cm^{-3} , respectively.

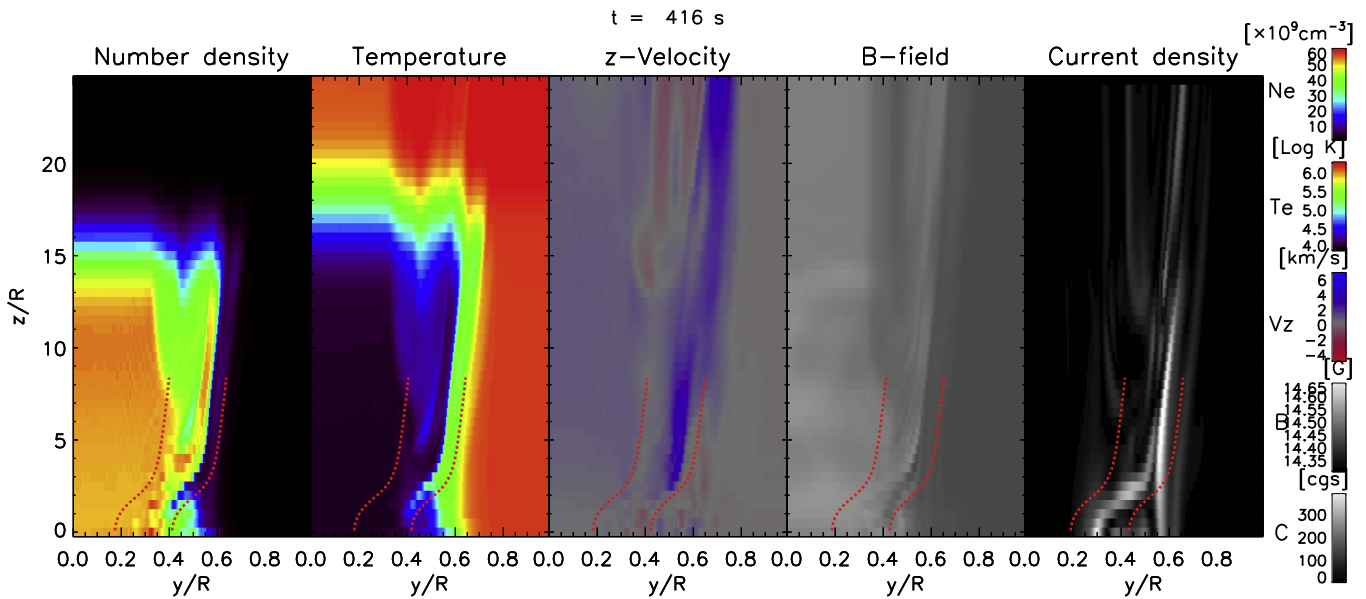


Figure 7. From left to right, a cut along the y - z plane at $x = 0$ for the number density, temperature, z -velocity, magnetic field strength, and current density for a particular snapshot in which an upward propagating twist is observed (marked between the red dotted curves). Blue and red in the z -velocity panel denote upward and downward velocities, respectively. See also the accompanying animation for this figure.

(An animation of this figure is available.)

A reshuffling of the magnetic field is produced by the TWIKH rolls, which increases and decreases the magnetic pressure around the boundary and toward the core, respectively. Ubiquitous current sheets along the flux tube, throughout most of the loop’s volume, are produced in this process. Due to the perpendicular gradient in the magnetic field imposed by the global standing kink mode, both the magnetic field strength and the currents are stronger toward the footpoints than in the rest of the flux tube. This effect, combined with the shearing from the TWIKH rolls, whose size and development increases with height, leads to strong currents that peak at the footpoint and are on average larger along the spicule than in the corona, as can be seen in Figure 6. The figure further shows that the KHI vortices introduce not only strand-like structure in density and temperature, but in the magnetic field as well, leading to filamentary current sheets over most of the flux tube.

4.2. Translating the Model Into Observable Quantities

4.2.1. Source Functions and Optical Depths

Since the lower levels for both the Mg II k and Ca II H lines are the ground states of their ions, to understand the dynamics observed in these lines we plot in Figure 8 the level populations of the ground states of singly ionized and doubly ionized species for the Mg and Ca atoms for the initial time. For Mg we find that at the edges of the flux tube there is a sizeable population of Mg III, but as the temperature drops inside the tube, most Mg is in the form of Mg II, a state that is kept throughout the simulation. This can be seen in the source function cross-section of Figure 9—nearly the whole tube contributes photons to the h and k lines. The optical depth at line center for these Mg lines is below 1 for rays going through the boundaries across the KHI vortices, but is on average above 1 for rays crossing through the core of the loop, as shown in Figure 10. During the simulation the optical depth varies significantly, and for rays crossing the loop core it can increase to values close to 40. This indicates that the Mg II k line is

generally optically thick in our model (at the chosen height of 11 Mm). On the other hand, most of the Ca in the flux tube exists in the doubly ionized state, Ca III. Only a few percent of atoms are in Ca II form, and those are predominantly found in a ring at the edges of the flux tube as shown in Figure 9. This region is the only significant contributor to the Ca II H line. The optical depth at line center for rays crossing the loop is well below 1 throughout the simulation. Therefore, the Ca II H line is very weak and optically thin.

It is important to note that the described appearance of the spicule in the Mg II k and Ca II H lines is strongly dependent on the initial condition of our model. For instance, it is likely that a spicule with lower densities will be optically thin in both of these lines, and with different chromospheric temperature ranges it is possible to significantly vary the element population in the core and boundaries, thereby modifying the shape of the respective source functions. In this work we opted for taking values representative of a typical spicule, since the forward modeling of a series of different models that a parameter space investigation would entail is beyond the present scope, and a very numerically demanding task. We also note that spicules present a highly dynamic environment in which the density may vary on short timescales with lines becoming optically thin and thick during the lifetime of the spicule. Therefore a word of caution is needed against straightforwardly generalizing our forward modeling results.

4.2.2. Strand-like Structure in Imaging and Spectra, and Propagating Twists

As shown by Figure 9, the large TWIKH rolls that appear after one period are observed as opposite large amplitude Doppler shifts and enhanced spectral line widths in the Mg II k line at the edges of the loop. This can be understood by the shape of the source function of this line, whose cross-section has a ring structure with peak values at the spicule edges. This, in turn, is due to contributions from wavelengths away from the

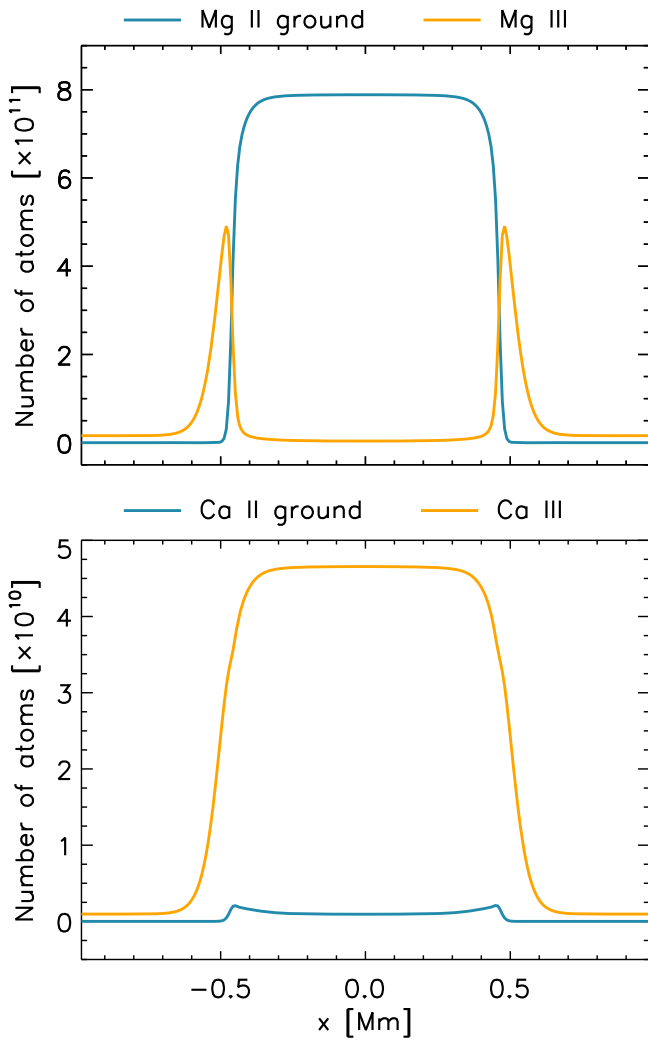


Figure 8. Populations of the ground states of the singly ionized and the doubly ionized species for Mg (upper panel) and Ca (lower panel) at the initial time of the simulation (no instability present).

line core, which contribute to the Mg II slit-jaw emission as observed with *IRIS* because of the broad *IRIS* transmission function. At the line core the source function is strong in both the edges and inside the tube, but at wavelengths in the line wings the source function is higher at the tube edges because there the regular line profiles are shifted into those wavelengths due to the large Doppler shifts in these regions that come from the KHI dynamics. Therefore, in our model, the Mg II source function captures well the KHI dynamics and, at the same time, is shaped by them. As for Mg II, the Si IV ion has a maximum emissivity around the edge of the vortices, where the temperature increases steeply from chromospheric to coronal values. The Mg II line has, however, also a contribution from the loop’s core, leading to a more opaque image compared to Si IV.

The Doppler velocity amplitudes are largest around the times of maximum displacement, where the vortices reach their largest size. The opposite Doppler velocities between the edges and the core are due to the fact that TWIKH rolls have, on average, a similar direction as the counterflow around the flux tube, which is contrary to that of the loop’s core (which moves according to the global kink mode).

Downward and upward propagating twists can be seen in the Si IV and Mg II intensity images of Figure 9 with speeds of up to 325 km s^{-1} (the Alfvén speed varies between 185 and 1285 km s^{-1} from the interior to the exterior of the spicule). These twists are associated with those identified in Figure 7.

As the vortices break up and new vortices appear, strand-like structure is generated along the spicule in intensity, Doppler velocity, and line width maps. All quantities shown in Figure 9 increase with height. For both the Mg II and Si IV line intensities, this is due to the sharp increase in temperature in the transition region (and corresponding decrease in density) which, under optically thin conditions (which applies to Mg II at the transition region densities), leads to higher intensity up to the maximum formation temperature ($10^{4.25} \text{ K}$ and 10^5 K for Mg II k and Si IV 1403, respectively).

4.2.3. Evolution of Spectra: Bursty Profiles for Chromospheric Lines

In Figure 11 we show the time–distance diagram for spectral quantities along a slit crossing the flux tube perpendicularly at a height of 11 Mm (red line in Figure 9). The LOS angle is 45° with respect to the axis of oscillation (white arrow in Figure 9). Results from the optically thin and radiative transfer approaches for the Mg II line are shown for comparison. The Doppler velocity and line width maps show similar behavior as previously reported for prominences and coronal loops (Antolin et al. 2015, 2017): that is, herringbone-shaped features in the Doppler maps, with Doppler shift sign changes starting at the loop edges, maximum values also at the loop edges (π out-of-phase with the plane-of-sky motion, as previously observed with *Hinode* and *IRIS*; Okamoto et al. 2015), and ragged transitions between consecutive blueshifts due to the TWIKH rolls. A sharp increase in line width (4 to 7 km s^{-1}) is observed accompanying the formation of the vortices.

The Si IV, Ca II and Mg II intensities show strand-like structures due to the TWIKH rolls, although the loop average intensity and the intensity variations are different for each. Due to the difference in opacity, the loop’s body appears mostly invisible in Si IV and similarly in Ca II, but is visible in Mg II, which is mostly optically thick. The TWIKH rolls’ intensity over time is rather constant in Si IV, with occasional bursts on a timescale of $\approx 50 \text{ s}$. However, the Mg II, and particularly the Ca II intensity is strongly bursty with bright features lasting ≈ 50 – 100 s .

In our model we find that the Doppler velocities in Mg II derived from the optically thin approximation generally agree with those derived from the radiative transfer approach, despite the presence of reversals in the line profile. This is mostly due to the ring shape of the source function, which indicates that most of the line profile is formed in the edge (and therefore optically thin) part of the flux tube, even for an LOS ray that crosses the loop core. Since the pixels on the opposite side of the loop along this LOS ray have, in general, a similar Doppler velocity (due to the kink mode symmetry), the contribution of these pixels (present in the optically thin approximation) does not significantly alter the centroid of the line. On the other hand, the line widths do differ between both approaches due to the presence of opacity broadening. The line widths from the radiative transfer calculations are in general larger than those from optically thin radiation by 2 – 3 km s^{-1} (50%–60%). The line profiles obtained from *IRIS* for case 1 exhibit on average few reversals, suggesting a spicule that is not as optically thick as the one considered in our model.

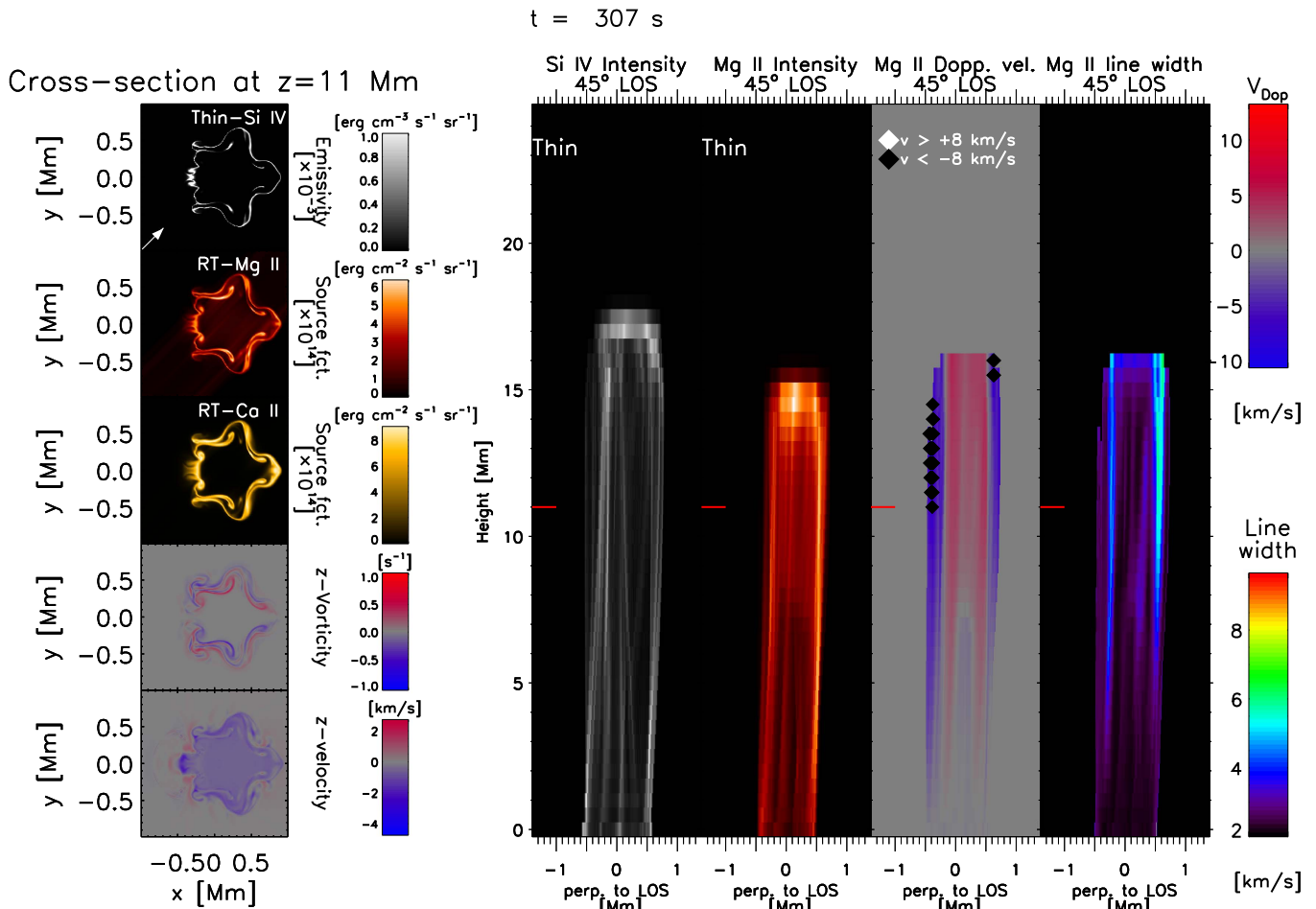


Figure 9. Spicule model. Four-set on right: side view of the simulated spicule at 45° line-of-sight (LOS) for the optically thin calculation (the LOS angle is defined in the plane perpendicular to the loop, with 0° matching the x direction, as in Antolin et al. 2017). The white/black symbols in the Doppler velocity panel indicate velocities above 8 km s^{-1} in magnitude. Five-set on left: from top to bottom, perpendicular cross-section of the spicule at a height of $z = 11 \text{ Mm}$ for the emissivity ($G_\lambda(T, n_{el})n_{el}^2$, with G , T , n_{el} the contribution function for the emission line, temperature, and electron number density) of Si IV 1402.77 \AA , the source functions for Mg II k and Ca II H, the z -component of the vorticity, and the z -component of the velocity. For the last, blue/red denotes upward/downward velocities. The arrow on the number density panel shows the 45° LOS direction.

(An animation of this figure is available.)

5. Discussion

5.1. Detailed Comparison with IRIS

To bring our numerical results closer to the observations we degrade the spatial, temporal, and spectral resolutions to those corresponding to the *IRIS* and *Hinode/SOT* observations. For the *IRIS* Mg II k line comparison we convolve the data spatially with the *IRIS* point-spread function (PSF). We then convolve the spectra with a Gaussian with a FWHM of 60 m\AA (approximate NUV resolution) and rebin to *IRIS* spectral pixel size. This is followed by spatial pixelization to the same platescale as *IRIS*. Lastly, we perform Gaussian fits to the spectra to obtain Doppler velocities and line widths. For comparison with observations with the SOT Ca II filter we integrate the Ca II H spectra over wavelength and apply the spatial convolution using a PSF with FWHM of $0''.22$, after which we rebin to the SOT platescale. For the temporal domain, we sum the numerical quantities for a number of snapshots matching roughly the time cadence of the instrument. Since the SOT exposure time is very short (similar to that of the numerical output), we only do the temporal integration for the *IRIS* forward modeling.

In Figure 12 we show the results of the forward modeling specified above. For better comparison we take an interval of time in the simulation similar to that observed (particularly in terms of wave periods, which is roughly 2), and show $\approx 100 \text{ s}$ into the simulation, which can be interpreted as the time taken by the spicule to move upwards, above the chromosphere (and become visible), and also the time since the start of the kink perturbation (which could be produced by the spicule generation mechanism itself; Martinez-Sykora et al. 2017). Furthermore, we assume that we are observing from an angle of 135° instead of the previously assumed 45° . This is only to match the observed alternation of Doppler shifts, starting from red, for case 1. Because of the symmetries of the kink mode, we expect minimal changes to the radiative transfer modeling from this change of angle. Comparing the numerical results with the observations in Figure 12 we can better distinguish the similarities and differences. The first obvious difference is the amplitude. Our modeled perturbation leads to roughly half (or less) of the observed displacement. The obtained Doppler velocities and line widths are also about half those observed. We would expect that for higher kink amplitudes in our model correspondingly higher velocities and line widths in the

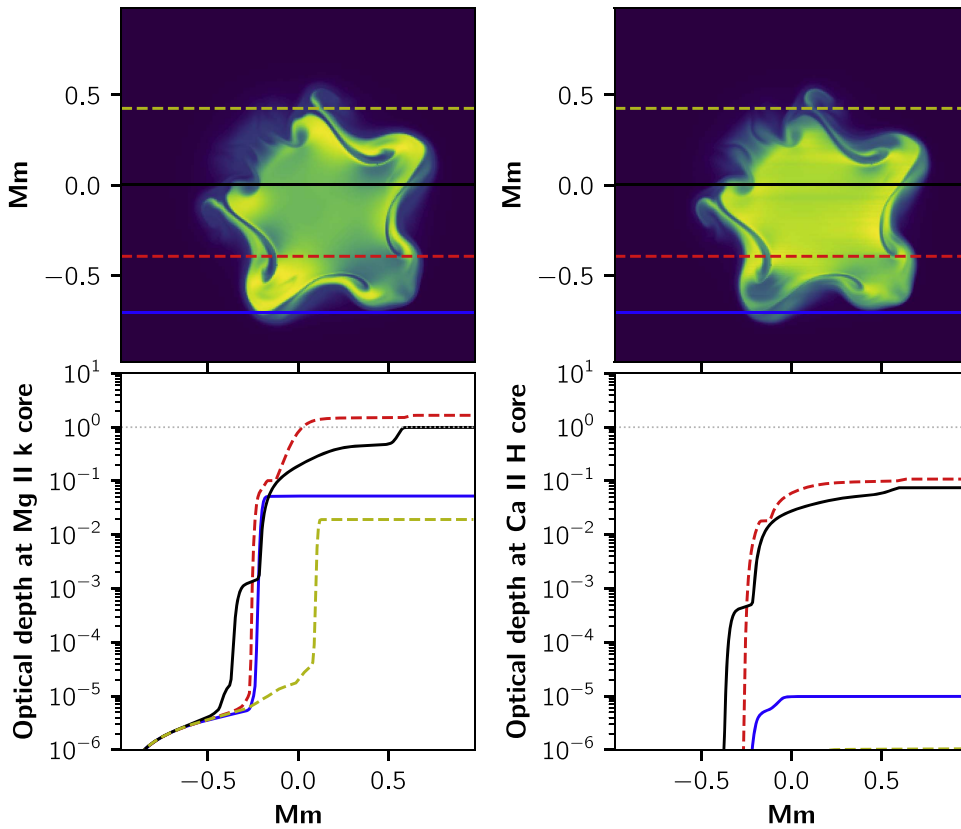


Figure 10. Opacity (upper panels) and optical depth (lower panels) for the Mg II k (left panels) and Ca II H lines (right panels). The solid blue, dashed red, solid black, and dashed yellow lines in the upper panels represent LOS rays crossing the loop (the background of the images corresponds to the logarithm of opacity at line center for each spectral line for the same snapshot as in Figure 9). The optical depth for each of these rays at this time in the simulation is shown in the lower panels. Optical depth unity is represented by the dotted gray line.

TWIKH rolls are obtained. There is also much more complexity in the Ca II and Mg II intensities and spectra from the observations, which seems to lead to a clear imbalance in the line widths between the left and right side of the spicule. Besides possible LOS interference from other structures, we also notice that the spicule group is about double the size of our model. The increase in size would, on one hand, be comparable to increasing the numerical resolution (if keeping the same number of grid points) which, as shown in Antolin et al. (2015) and Magyar & Van Doorselaere (2016), brings in myriad additional vortices of multiple sizes (vortices within vortices recalling a fractal geometry). On the other hand, a larger size also means a larger velocity shear at the boundaries for the same perturbation amplitude, which would more readily trigger the KHI. These effects would therefore increase the complexity in the imaging and spectral quantities and bring the model closer to observations.

Nonetheless, several of the observed features of case 1 in Figure 2 and case 2 in Figure 3 (and previously reported) with *Hinode* and *IRIS* of spicules can be reproduced with the model: the strand-like structure, the collective behavior among the strands, the (qualitative) variation in Ca II and Mg II intensities, the ragged Doppler shift transitions and, to a lower extent, the accompanying line width increase. The collective behavior observed at high resolution in Ca II H (in Figure 2) among the strand-like structure opens an interesting question on the nature of the spicule. Is it the single-strand structure or the set of strands, seen as a monolithic structure in the coarser resolution of *IRIS* and at higher opacity in the Mg II line? The collective

motion suggests the latter, belonging to a flux tube entity which is mostly invisible in the Ca II H line (Skogsrud et al. 2015). This is supported by the possibility that many of the observed strands in intensity and in Doppler maps may actually be TWIKH rolls, as our model suggests.

5.2. Higher-resolution Observations: Stranded Structure in Spectra

Higher-resolution observations with CRISP at the SST indicate the sudden appearance/disappearance of, and short-lived, strand-like structure in the Doppler shifts across spicule-like features, even with opposite signs for adjacent strands (Kuridze et al. 2015; Pereira et al. 2016; Shetye et al. 2016; Srivastava et al. 2017). Such features are perhaps the observed features that are best reproduced from this model once the KHI develops after roughly one wave period (Figures 9 and 11). This strand-like structure in Doppler is even more distinct in the Si IV line, as shown in Figure 13. In our model, the Si IV line maps a slightly outer layer of the flux tube, and therefore one in which the azimuthal Alfvén waves travel at higher speeds and the Doppler shifts have higher frequency. Doppler shift variations with a period of ≈ 50 – 100 s can be seen at small scales. At the coarser resolution of *IRIS* (Figure 12) the strand-like structure in the Doppler maps is not observed, and only a ragged transition in time between opposite Doppler shifts remains, matching well the observed Doppler shift change in case 1. The TWIKH rolls develop after about one period, in agreement with the observed time interval in Figure 2 from the

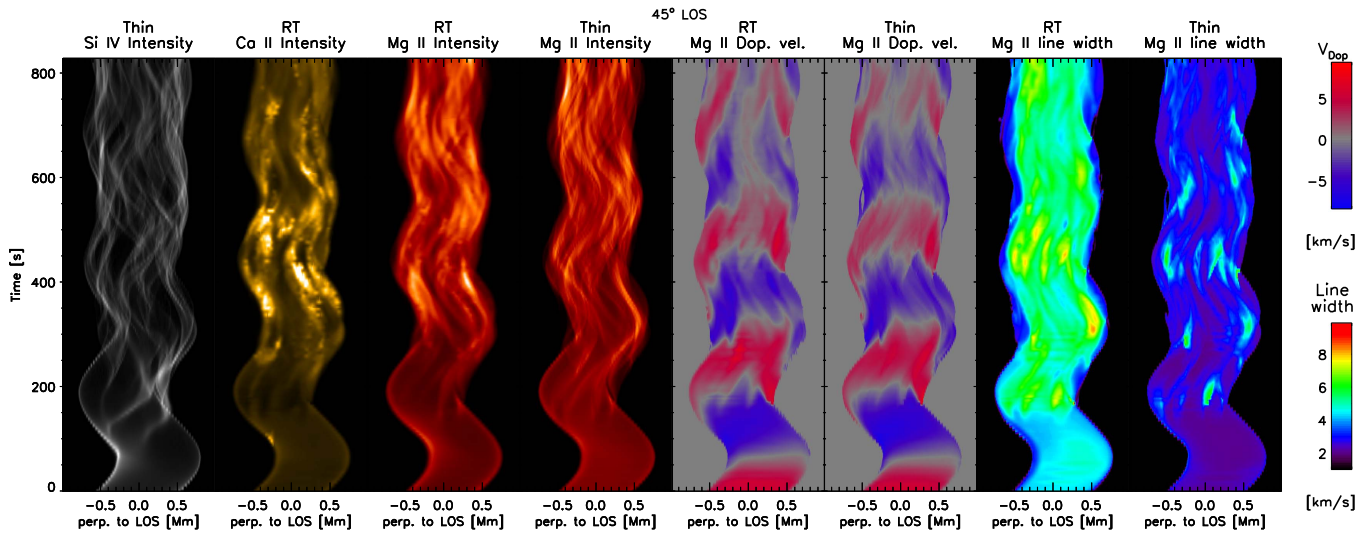


Figure 11. Time–distance diagrams at 45° LOS for the cross-section cut at $z = 11$ Mm indicated in Figure 7 for several quantities (indicated on the top) and for optically thin (“Thin”) and radiative transfer (“RT”) calculations.

moment the oscillating spicule appears until the time of maximum strand formation and intensity.

5.3. Bursty, Doubly Periodic Line Profiles

To further inspect the similarities and differences in the temporal variation of intensity we integrate over the spicule width the Ca II, Mg II, and Si IV intensities, and show the resulting light curves in Figure 14. For the observations, besides the integrated Mg II k intensity at the slit position, we also show the Ca II H, SJI 2796 and 1400 filter intensities averaged along the spicule from the slit position to a height of 4 Mm. This is done in order to reduce the possible LOS interference of other structures at lower heights as well as small-scale longitudinal inhomogeneities, and allows us to focus on effects that have a long scale height (such as the global kink mode and the TWIKH rolls). From Figure 14 we can see that the integrated Mg II k intensity has stronger variability than the SJI 2796 intensity, which is expected because of the single slit position, but both lines follow roughly the same trend and are roughly in-phase with the spicule’s transverse displacement. The fact that both lines follow the same trend is a reassurance that most of the captured signal at the *IRIS* slit position in the observations comes indeed from the spicule of interest, and not from other structures along the LOS.

To some extent, the strong variability in Ca II H, matching the previously reported appearance and disappearance of strands in this line, and the accompanying increase in Mg II k intensity (and SJI 2796), are well reproduced in the numerical model. The SJI 1400 light curve shows very little increase for case 1, and a decrease at the end of the time series is observed in all light curves, corresponding to a general fade-out during the downward motion of the spicule. This small intensity increase in Si IV seems to be captured by the numerical model. In our model we observe a clear in-phase intensity increase for all light curves, with a period of half that of the kink mode and with an offset of roughly $\frac{\pi}{2}$ from the maximum transverse displacement of the spicule, coinciding with times of maximum velocity shear. This offset is associated with the formation of the TWIKH rolls (Antolin et al. 2017). However, in case 1 the in-phase behavior between light curves is not clear. While initially a similar trend is observed between Mg II, Ca II H, and

Si IV, the subsequent strong increase in Ca II seems to break the in-phase behavior. The presence of periodicity with a period half that of the kink mode is also unclear.

5.4. Heating or Just Mixing?

In most reported cases an increase in SJI 1400 intensity is found, following the increase in cooler chromospheric lines, unlike the observed very mild increase of case 1 (Skogsrud et al. 2015). Indeed, previous and recent work indicates a transition region and coronal response to spicules, observed not only as an increase in Si IV emission but also in the coronal filters of AIA, suggesting heating (De Pontieu et al. 2011, 2017a). These results have been explained from a 2.5D radiative MHD model, in which similar features are obtained from the combination of propagating currents and heating fronts (De Pontieu et al. 2017b). In these models tangled fields are generated in the photosphere or below and ambipolar diffusion allows those fields, normally too weak to emerge into the atmosphere, to emerge and release the magnetic tension. High-amplitude Alfvénic waves are produced, which nonlinearly generate strong enough slow-mode shocks that drive material upwards, thereby forming a spicule. These Alfvénic perturbations propagate along the spicule and corona, heating up the plasma. The combination of slow-mode shocks, longitudinal flows, and Alfvénic perturbations leads to coronal propagating disturbances and generation of coronal strands that are similar to those observed. Although the resistivity in the spicule and chromosphere are captured well by the ambipolar resistivity in that model (which is higher than the numerical resistivity in the spicule), the obtained Alfvénic wave dissipation in the coronal parts of the model is strongly dependent on the resistivity, which is much higher than the expected coronal resistivity. The model presented here shows that Alfvénic waves such as transverse MHD waves can further lead to TWIKH rolls.

Our model is purely adiabatic, and therefore there is no heat exchange between adjacent fluid elements. The obtained intensity variability is due to compression and mixing from the TWIKH rolls of inner (colder) with outer (hotter) material. Our results therefore require caution when interpreting observations, since we can obtain similar intensity

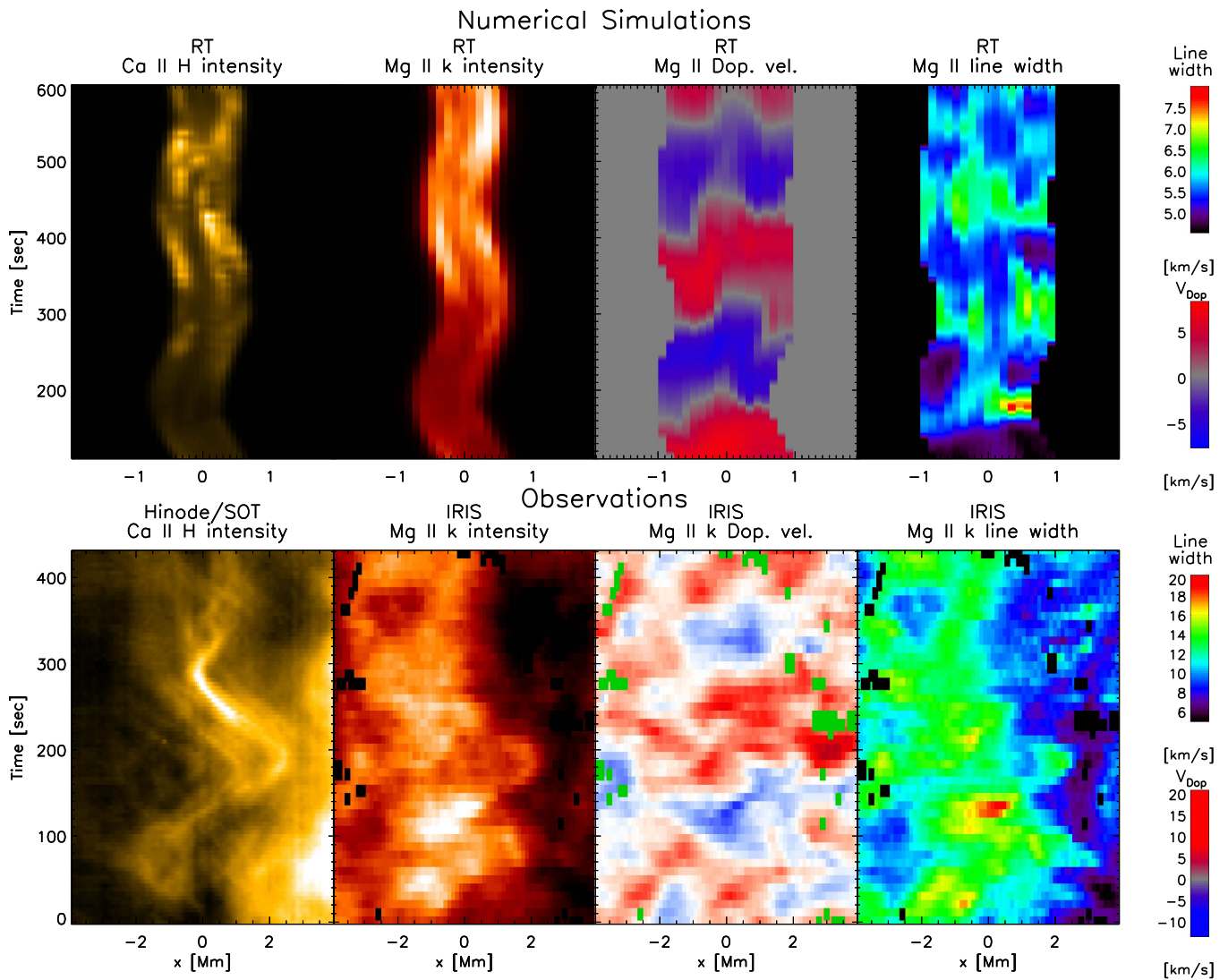


Figure 12. Comparison of *Hinode/IRIS* observations with simulation results. We forward model the numerical results with a radiative transfer approach and degrade the resolution targeting the *IRIS* and *Hinode* spatial, temporal, and spectral resolutions. For the sake of comparison, we take the same temporal interval (in terms of wave oscillation periods) as in the observations and change the sign of the Doppler velocities, which would correspond to a viewing angle of 135° .

enhancements in chromospheric lines which are not caused by actual heating. While a time-lag in intensity increase is usually observed from chromospheric to transition region lines (interpreted as heating), the TWIKH rolls in our model lead to in-phase variation of the intensity between chromospheric and transition region lines. TWIKH rolls are compressive and locally enhance the plasma density adiabatically. On average, the rolls enhance the magnetic field around the boundary layer, which is at the same time decreased within the flux tube. Correspondingly, the internal energy is decreased around the boundary layer and increased within the flux tube. The obtained variation of intensity, and particularly its increase within a TWIKH roll, does not strictly correspond to heating from wave dissipation (Antolin et al. 2017). Our model, however, shows that TWIKH rolls enhance the currents through the bending, reshuffling, and twisting of magnetic field lines, suggesting that such TWIKH rolls can lead to heating. Indeed, in similar but more realistic resistive (and viscous) models (Karampelas et al. 2017), and resistive but higher resolution (leading to well developed turbulence; Antolin et al. 2015), or with anomalous resistivity (simulating

energy deposition at smaller scales due to turbulence; Howson et al. 2017b) wave dissipation is achieved. It is, however, still unclear whether significant heating would take place to counter radiative and conduction losses. The addition of twist in the flux tube as an initial condition, even if small, although suppressing to some extent the TWIKH rolls (Soler et al. 2010; Terradas et al. 2017), would also produce more energetic ones, due to the addition of an azimuthal component in the field (Howson et al. 2017a). The TWIKH rolls from our model or one with twist (in which case they would be helical) may also explain the vortex motions observed around chromospheric jets (Kuridze et al. 2016). The higher energies in the twisted scenario would likely lead to stronger field-aligned flows (Yokoi & Brandenburg 2016). We have shown that the twists and currents that accompany the TWIKH rolls in our model generate Alfvénic propagating disturbances along the spicule with significant energy. It is unclear, however, whether such disturbances would be able to heat the corona in a more realistic model. In an extended 3D MHD model from that of Martinez-Sykora et al. (2017) but with higher spatial resolution, similar to that in our model, we would expect a

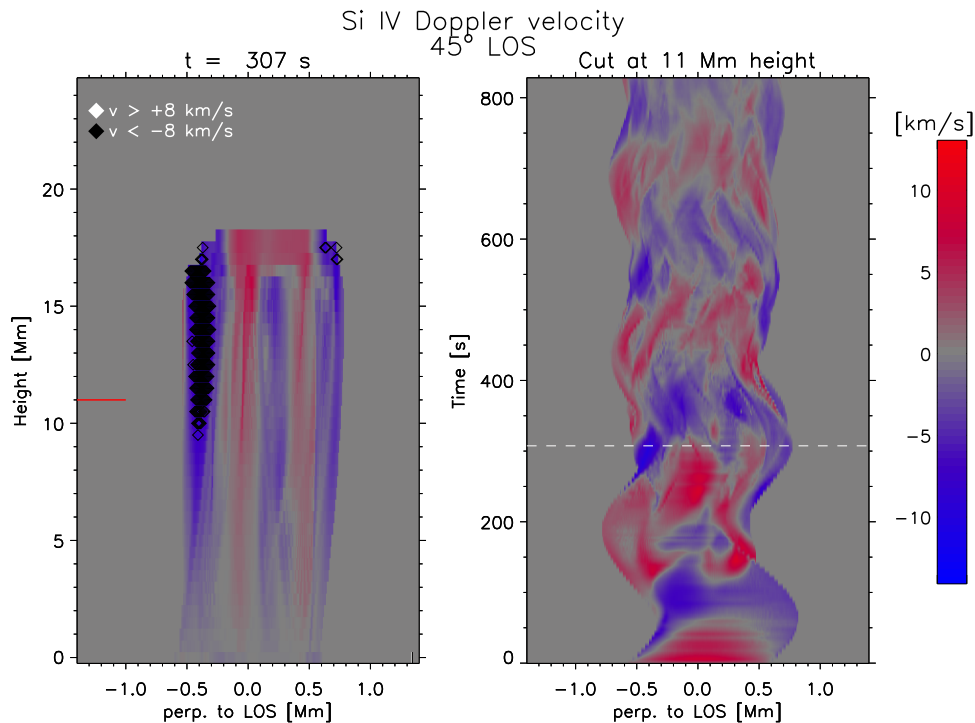


Figure 13. Doppler velocity in the Si IV line for an LOS of 45° . In the left panel the Doppler velocity map is shown for the same snapshot as in Figure 9, where the black (and white) diamonds indicate speeds above 8 km s^{-1} in magnitude. In the right panel we show the time–distance diagram for a cut at a height of 11 Mm (red line on the left panel).

(An animation of this figure is available.)

combination of the described effects. Our model suggests that TWIKH rolls would be produced by the transverse perturbations that accompany the spicule generation mechanism. This combination would therefore not only explain the spicule generation but also its multi-strand morphology in intensity and spectra, and further support the accompanying heating at the transition region and coronal temperatures from that model.

5.5. TWIKH Rolls in Coronal Loops, Prominences, and Spicules

Besides spicules as in the present work, the TWIKH rolls model has been tested in other, very different, plasma environments of the solar atmosphere: prominences (Antolin et al. 2015) and coronal loops (Antolin et al. 2014, 2017). The major parameter differentiating each model is the density contrast: $\rho_i/\rho_e = 50, 10, 3$, respectively for the spicule, prominence, and the coronal loop. The onset time of the TWIKH rolls increases with the density and the velocity shear amplitude, as expected from theory. The higher the density of the structure, the higher the inertia and subsequent deformation of the flux tube. In the prominence, and particularly in the spicule cases, we observe, additionally to the KHI, rolls that develop at the wake displaying characteristic Rayleigh–Taylor features, which help in the subsequent generation of turbulence.

In all three cases TWIKH rolls play a major role in the appearance of the structure in the EUV, transition region, or chromospheric wavelengths, with the characteristic strand-like structure. Due to the higher phase speeds at the edges of the loop (leading to phase mixing) the Doppler maps display alternating blue/redshift herringbone shapes, and the TWIKH rolls appear as red/blueshifted intrusions in the main blue/redshifted signal of the flux tube’s body. These intrusions are

visible at high resolution, and the forward modeling performed here shows that they should be observable at *IRIS* resolution, offering an explanation for the small-scale features in case 1.

Higher resolution allows more wave dissipation in our numerical model, due to better developed turbulence (Antolin et al. 2015). Setting the spatial resolution factor aside, we have shown that the mixing can play an important role in the observed morphology. Since this mechanism depends on the temperatures and densities present initially, the end result can be significantly different. This is illustrated by the coronal, prominence, and spicule models (comparing only those at same spatial resolution): for similar perturbation amplitudes and for the same temperature contrast, the population of the “mixed” material will have lower intermediate temperatures for higher density contrast. For instance, we would expect a higher Si IV population at the end state by taking a lower density contrast in the spicule model (as indicated by the prominence model).

6. Conclusions

Having analyzed *Hinode* and *IRIS* observations of several spicules, we found significant differences between them: cases with a fixed Doppler shift transition along the spicule axis and little coherence of strands best match rotation or propagating long-wavelength torsional Alfvén wave models. Cases with a Doppler shift transition at maximum displacement and strong strand coherence best match the kink wave model. The latter is confirmed with a 3D MHD numerical and radiative transfer forward modeling of a spicule oscillating with a transverse MHD wave. TWIKH rolls are rapidly produced and can explain several of the observed features: coherent strand-like structure in intensity, Doppler velocities and line widths at high resolution, and ragged Doppler shift sign changes at maximum

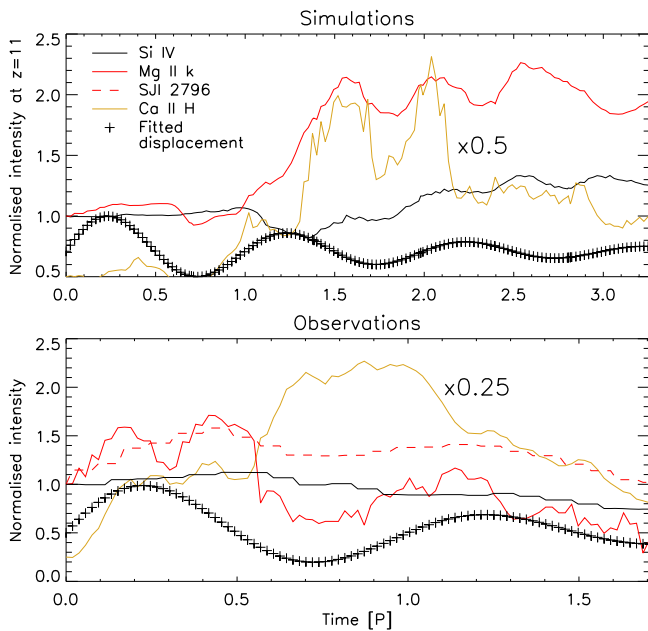


Figure 14. Light curves integrated over the spicule width for the Ca II H, Mg II k, and Si IV lines for the simulation (upper panel) and observations (lower panel; we show both the Mg II k and SJI 2796 light curves, besides the SJI 1400 light curve from *IRIS*). To reduce the contribution from other features along the LOS, for the SOT and SJI quantities we integrate also in the vertical direction, from the slit position up a height of 4 Mm). The SOT light curve values are multiplied by a half and a quarter in the top and bottom panels, respectively, for better comparison with the other light curves. The x-axis represents time in units of the wave period, 255 s and 250 s, in the model and observations, respectively. An exponentially decaying cosine has been fitted to the observed SOT displacement in the time–distance diagrams (fitting the maximum intensity crosses in Figure 2) and also to the time–distance diagram of the Mg II intensity map from the simulation. The fits are overlaid (with ad hoc amplitudes) as crosses for each time step.

displacement accompanied by increased line widths. The rapid temperature variations from the mixing and the TWIKH rolls’ short lifetimes produce strong variations in Doppler velocity and in the Ca II H intensity, in agreement with the observed sudden appearance and disappearance of spicule strands in chromospheric lines, but not matching the clear preference for fading in cooler lines and appearance in hotter lines. This model can explain particularly well the Doppler maps from high-resolution instruments with tunable wavelength filters such as *SST/CRISP*, where spicules show up as contiguous opposite Doppler shifts (strand-like structure in Doppler maps) that appear and disappear at high frequency. Rather than the individual strand being called a spicule, our model suggests that the collection of such strand-like structure should be considered as one spicule, belonging to the same flux tube that is subject to a transverse MHD mode. The TWIKH rolls also lead to twists and currents that propagate along the spicule at Alfvénic speeds. The increase in temperature in our model only results from adiabatic effects, which are unable to generate the observed intensity increase in higher-temperature lines, suggesting that an additional mechanism must be at work. This is not surprising given the simplicity of our model, and results from the more realistic 2.5D MHD model of Martínez-Sykora et al. (2017) indicate already that spicule-like features are likely to involve a variety of complex mechanisms that are not included here. However, our higher-resolution model indicates that the small-scale processes triggered by dynamic instabilities

associated with transverse MHD waves may also play a significant role in the observed spicule features.

We would like to thank the anonymous referee for valuable comments and suggestions that led to an improvement of this manuscript. This research has received funding from the UK Science and Technology Facilities Council (Consolidated Grant ST/K000950/1) and the European Union Horizon 2020 research and innovation programme (grant agreement No. 647214), and also from JSPS KAKENHI Grant Numbers 25220703 (PI: S. Tsuneta). T.P. acknowledges support by the Research Council of Norway through its Centres of Excellence scheme, project number 262622, and through grants of computing time from the Programme for Supercomputing. Numerical computations were carried out on Cray XC30 at the Center for Computational Astrophysics, NAOJ, and at the Pleiades cluster through computing project s1061 from NASA’s High-End Computing Program. *Hinode* is a Japanese mission developed and launched by ISAS/JAXA, with NAOJ as domestic partner and NASA and STFC (UK) as international partners. It is operated by these agencies in cooperation with ESA and NSC (Norway). *IRIS* is a NASA small explorer mission developed and operated by LMSAL with mission operations executed at NASA Ames Research center and major contributions to download communications funded by ESA and the Norwegian Space Centre.

ORCID iDs

P. Antolin <https://orcid.org/0000-0003-1529-4681>
 T. M. D. Pereira <https://orcid.org/0000-0003-4747-4329>
 B. De Pontieu <https://orcid.org/0000-0002-8370-952X>
 I. De Moortel <https://orcid.org/0000-0002-1452-9330>

References

- Ajabshirizadeh, A., Ebadi, H., Vekalati, R. E., & Molaverdikhani, K. 2015, *Ap&SS*, 357, 33
- Antolin, P., De Moortel, I., Van Doorselaere, T., & Yokoyama, T. 2017, *ApJ*, 836, 219
- Antolin, P., Okamoto, T. J., De Pontieu, B., et al. 2015, *ApJ*, 809, 72
- Antolin, P., Yokoyama, T., & Van Doorselaere, T. 2014, *ApJL*, 787, L22
- Arregui, I. 2015, *RSPTA*, 373, 20140261
- Arregui, I., Oliver, R., & Ballester, J. L. 2012, *LRSP*, 9, 2
- De Moortel, I., & Nakariakov, V. M. 2012, *RSPTA*, 370, 3193
- De Pontieu, B., Carlsson, M., Rouppe van der Voort, L. H. M., et al. 2012, *ApJL*, 752, L12
- De Pontieu, B., De Moortel, I., Martínez-Sykora, J., & McIntosh, S. W. 2017a, *ApJL*, 845, L18
- De Pontieu, B., Erdélyi, R., & De Moortel, I. 2005, *ApJL*, 624, L61
- De Pontieu, B., Martínez-Sykora, J., & Chintzoglou, G. 2017b, *ApJL*, 849, L7
- De Pontieu, B., McIntosh, S., Hansteen, V. H., et al. 2007a, *PASJ*, 59, 655
- De Pontieu, B., McIntosh, S. W., Carlsson, M., et al. 2007b, *Sci*, 318, 1574
- De Pontieu, B., McIntosh, S. W., Carlsson, M., et al. 2011, *Sci*, 331, 55
- De Pontieu, B., McIntosh, S. W., Hansteen, V. H., & Schrijver, C. J. 2009, *ApJL*, 701, L1
- De Pontieu, B., Rouppe van der Voort, L., McIntosh, S. W., et al. 2014a, *Sci*, 346, D315
- De Pontieu, B., Title, A. M., Lemen, J. R., et al. 2014b, *SoPh*, 289, 2733
- Goossens, M., Andries, J., & Aschwanden, M. J. 2002, *A&A*, 394, L39
- Gruszecki, M., Nakariakov, V. M., van Doorselaere, T., & Arber, T. D. 2010, *PhRvL*, 105, 055004
- He, J., Marsch, E., Tu, C., & Tian, H. 2009, *ApJL*, 705, L217
- Howson, T. A., De Moortel, I., & Antolin, P. 2017a, *A&A*, 607, A77
- Howson, T. A., De Moortel, I., & Antolin, P. 2017b, *A&A*, 602, A74
- Iijima, H., & Yokoyama, T. 2017, *ApJ*, 848, 38
- Jess, D. B., Pascoe, D. J., Christian, D. J., et al. 2012, *ApJL*, 744, L5
- Judge, P. G., Reardon, K., & Cauzzi, G. 2012, *ApJL*, 755, L11
- Karampelas, K., Van Doorselaere, T., & Antolin, P. 2017, *A&A*, 604, A130
- Kosugi, T., Matsuzaki, K., Sakao, T., et al. 2007, *SoPh*, 243, 3

- Kudoh, T., Matsumoto, R., & Shibata, K. 1999, *Computational Fluid Dynamics Journal*, 8, 56
- Kuridze, D., Henriques, V., Mathioudakis, M., et al. 2015, *ApJ*, 802, 26
- Kuridze, D., Zaqarashvili, T. V., Henriques, V., et al. 2016, *ApJ*, 830, 133
- Leenaarts, J., Pereira, T., & Uitenbroek, H. 2012, *A&A*, 543, A109
- Leenaarts, J., Pereira, T. M. D., Carlsson, M., Uitenbroek, H., & De Pontieu, B. 2013a, *ApJ*, 772, 89
- Leenaarts, J., Pereira, T. M. D., Carlsson, M., Uitenbroek, H., & De Pontieu, B. 2013b, *ApJ*, 772, 90
- Magyar, N., & Van Doorselaere, T. 2016, *ApJ*, 823, 82
- Magyar, N., Van Doorselaere, T., & Goossens, M. 2017, arXiv:1702.02346
- Martínez-Sykora, J., De Pontieu, B., Hansteen, V. H., Rouppe van der Voort, L. H. M., & Pereira, T. M. D. 2017, *Sci*, 356, 1269
- Martínez-Sykora, J., De Pontieu, B., Leenaarts, J., et al. 2013, *ApJ*, 771, 66
- Narang, N., Arbacher, R. T., Tian, H., et al. 2016, *SoPh*, 291, 1129
- Okamoto, T. J., Antolin, P., De Pontieu, B., et al. 2015, *ApJ*, 809, 71
- Okamoto, T. J., Liu, W., & Tsuneta, S. 2016, *ApJ*, 831, 126
- Pereira, T. M. D., De Pontieu, B., & Carlsson, M. 2012, *ApJ*, 759, 18
- Pereira, T. M. D., De Pontieu, B., Carlsson, M., et al. 2014, *ApJL*, 792, L15
- Pereira, T. M. D., Rouppe van der Voort, L., & Carlsson, M. 2016, *ApJ*, 824, 65
- Pereira, T. M. D., & Uitenbroek, H. 2015, *A&A*, 574, A3
- Rouppe van der Voort, L., De Pontieu, B., Pereira, T. M. D., Carlsson, M., & Hansteen, V. 2015, *ApJL*, 799, L3
- Sekse, D. H., Rouppe van der Voort, L., De Pontieu, B., & Scullion, E. 2013, *ApJ*, 769, 44
- Shetye, J., Kuridze, D., Stangalini, M., et al. 2016, *A&A*, 589, A3
- Skogsrud, H., Rouppe van der Voort, L., & De Pontieu, B. 2014, *ApJL*, 795, L23
- Skogsrud, H., Rouppe van der Voort, L., De Pontieu, B., & Pereira, T. M. D. 2015, *ApJ*, 806, 170
- Soler, R., Terradas, J., Oliver, R., Ballester, J. L., & Goossens, M. 2010, *ApJ*, 712, 875
- Srivastava, A. K., Shetye, J., Murawski, K., et al. 2017, *NatSR*, 7, 43147
- Suematsu, Y., Ichimoto, K., Katsukawa, Y., et al. 2008a, in *ASP Conf. Ser.* 397, *First Results From Hinode*, ed. S. A. Matthews, J. M. Davis, & L. K. Harra (San Francisco, CA: ASP), 27
- Suematsu, Y., Tsuneta, S., Ichimoto, K., et al. 2008b, *SoPh*, 249, 197
- Terradas, J., Andries, J., Goossens, M., et al. 2008, *ApJL*, 687, L115
- Terradas, J., Magyar, N., & Van Doorselaere, T. 2017, arXiv:1712.06955
- Tian, H., DeLuca, E. E., Cranmer, S. R., et al. 2014, *Sci*, 346, 1255711
- Tomczyk, S., McIntosh, S. W., Keil, S. L., et al. 2007, *Sci*, 317, 1192
- Tsiropoula, G., Tziotziou, K., Kontogiannis, I., et al. 2012, *SSRv*, 169, 181
- Tsuneta, S., Ichimoto, K., Katsukawa, Y., et al. 2008, *SoPh*, 249, 167
- Uitenbroek, H. 2001, *ApJ*, 557, 389
- Van Doorselaere, T., Antolin, P., Yuan, D., Reznikova, V., & Magyar, N. 2016, *FrASS*, 3, 4
- Yokoi, N., & Brandenburg, A. 2016, *PhRvE*, 93, 033125
- Zaqarashvili, T. V., Zhelyazkov, I., & Ofman, L. 2015, *ApJ*, 813, 123
- Zhelyazkov, I., Zaqarashvili, T. V., Chandra, R., Srivastava, A. K., & Mishonov, T. 2015, *AdSpR*, 56, 2727